Computational Condensed Matter 48 (2026) e01365

Contents lists available at ScienceDirect

Computational Condensed Matter

journal homepage: www.elsevier.com/locate/cocom

Full length article

Bismutite bulk and surface properties from density-functional theory

W. Elaggoune [a,*], I.A. Ruiz Alvarado [a], G. Grundmeier [b], W.G. Schmidt [a]

[a] Lehrstuhl für Theoretische Materialphysik, Universität Paderborn, Paderborn, 33095, Germany
[b] Lehrstuhl für Technische und Makromolekulare Chemie, Universität Paderborn, Paderborn, 33095, Germany

ARTICLE INFO

Keywords:
Bismutite ($Bi_2O_2CO_3$)
DFT
Excitonic effects
ab initio thermodynamics
Surface termination
Phase diagram

ABSTRACT

We investigate the structural, thermodynamic, and electronic properties of bismutite (bismuth subcarbonate, $Bi_2O_2CO_3$) using density-functional theory. A systematic comparison of the commonly assumed *Imm2* structure with the lower-symmetry $Pna2_1$ phase identifies the latter as the energetically favored bulk ground state. Hybrid-functional calculations including spin–orbit coupling yield a direct band gap of about 3 eV for the $Pna2_1$ structure, in good agreement with experiment, whereas the *Imm2* phase exhibits a significantly smaller indirect gap. The optical response is anisotropic and strongly influenced by excitonic effects. The (001) surface is analyzed using slab models in combination with *ab initio* thermodynamics. Under ambient conditions, a CO_3-terminated surface is found to be thermodynamically stable and electronically passivated, i.e., free of mid-gap states. In contrast, Bi-, O-, and Bi_2O_2-terminated surfaces become stable under reduced oxygen and/or carbon dioxide chemical potentials and exhibit pronounced surface states that pin the Fermi level within the bulk band gap. These states originate from undercoordinated surface atoms and are accompanied by substantial structural relaxations. Our results provide a consistent microscopic description of bulk and surface properties of $Bi_2O_2CO_3$ and establish a link between preparation conditions, surface stability, and electronic structure.

1. Introduction

Bismuth oxides exhibit exceptional structural versatility that has long fascinated solid-state chemists. A defining feature of bismuth oxides is the stereochemical activity of the $6s^2$ lone pair of Bi^{3+}, first emphasized by Andersson and Åström, which occupies a volume comparable to an anion and induces pronounced distortions in the local coordination environment [1]. Unlike typical trivalent cations that favor symmetric environments, Bi^{3+} exploits this activity to stabilize low-symmetry, layered architectures, endowing bismuth oxides with remarkable structural diversity. This lone-pair-driven flexibility underpins the rich polymorphism of Bi_2O_3, which adopts at least six distinct forms—α (monoclinic), β (tetragonal), γ (body-centered cubic), δ (face-centered cubic), ε (orthorhombic), and ω (triclinic)—with relative stability highly sensitive to temperature, atmosphere, and synthesis pathway [2].

Among these polymorphs, monoclinic α-Bi_2O_3 defines the thermodynamic ground state under ambient conditions. In contrast, the metastable tetragonal β-Bi_2O_3 plays a pivotal role in layered bismuth chemistry [3]. Despite its inherent instability, the β phase provides the recurring $[Bi_2O_2]^{2+}$ slab that links simple binary oxides to the complex architectures of multinary Sillén- and Aurivillius-type oxysalts [4–6]. Far from being a transient phase, β-Bi_2O_3 serves as a structural archetype underlying the structural diversity of layered bismuth oxysalts.

This role is most clearly revealed in the organization of bismuth oxysalts, where the $[Bi_2O_2]^{2+}$ slab is conserved while the interlayer chemistry varies. Two principal families crystallize around this motif. In Aurivillius phases, $[Bi_2O_2]^{2+}$ layers alternate with perovskite-like blocks, whereas in Sillén phases, the slabs are separated by anionic layers composed of halides or molecular groups [4,7]. Initially formulated for bismuth oxyhalides, the Sillén concept was subsequently expanded to carbonate-, ketterite-, and related systems, as well as structurally analogous compounds based on Pb, W, and Sb [8,9]. Across this broader family, the layered topology is preserved, but the chemical identity, orientation, and ordering of interlayer anions subtly reshape the symmetry, lattice distortions, and long-range structural coherence.

Bismutite exemplifies the profound consequences of this minimal chemical modification. Structurally, it represents a small departure from the β-Bi_2O_3 scaffold: the $[Bi_2O_2]^{2+}$ slabs are retained, while charge neutrality is achieved through the insertion of carbonate layers rather than extended oxide connectivity. Yet this subtle substitution fundamentally alters the structural framework. Early single-crystal studies by Grice indicated tetragonal diffraction metrics, but strict tetragonal symmetry led to stereochemical inconsistencies [10]. Subsequent neutron diffraction by Greaves and Blower revealed additional

* Corresponding author.
E-mail address: elgwarda@mail.uni-paderborn.de (W. Elaggoune).

https://doi.org/10.1016/j.cocom.2026.e01365
Received 19 May 2026; Received in revised form 8 June 2026; Accepted 9 June 2026
Available online 12 June 2026

reflections incompatible with a tetragonal cell, necessitating a larger orthorhombic description and suggesting orientational ordering of CO_3^{2-} groups [11]. The partial disorder of these carbonate units complicates refinement and long obscured the true crystallographic ground state, leaving the bulk symmetry of $Bi_2O_2CO_3$ uncertain for decades [12–14]. Theoretical studies assume the orthorhombic *Imm2* space group in modeling bismutite [12,13,15–19], while both neutron and electron diffraction indicate that the lower-symmetry $Pna2_1$ structure offers a more faithful description of the material [11,14]. To our knowledge, a systematic computational comparison of these two structures is still lacking. This is remarkable, given that bismutite is widely studied for its photocatalytic properties, particularly in the degradation of organic pollutants in water under UV or visible light [13,17,19–23]. It is also used in environmental remediation and as a component in catalysts due to its layered structure and chemical stability [24–27]. Additionally, it has potential applications in energy-related fields, such as in the development of photoelectrochemical systems and advanced functional materials [28–31].

The structural kinship between $Bi_2O_2CO_3$ and β-Bi_2O_3 is intimate. Both share identical $[Bi_2O_2]^{2+}$ layers, which facilitates facile and often reversible interconversion between the two phases [32,33]. Consistently, β-Bi_2O_3 reacts readily with atmospheric CO_2 at room temperature to form $Bi_2O_2CO_3$, while thermal treatment of $Bi_2O_2CO_3$ at 400 °C releases CO_2 and regenerates the β phase [11,34,35]. The layered architecture of bismutite introduces a pronounced anisotropy in surface stability [7] and explains the frequent plate-like morphologies dominated by basal facets [23]. The $[Bi_2O_2]^{2+}$ slabs and CO_3^{2-} layers stack along the crystallographic c axis, rendering the (001) planes as natural cleavage surfaces that terminate either the bismuth–oxygen slab or the carbonate layer [22,36–40]. However, unlike β-Bi_2O_3, where the high surface energy of (001) rationalizes limited exposure [41,42], the stability of the various conceivable bismutite (001) surface terminations has not yet been explored.

These knowledge gaps motivate the present study. Total-energy calculations and *ab-initio* thermodynamics are used to determine the bismutite bulk and surface ground state structures. Based on the relaxed atomic geometries, the bulk and surface electronic structure is calculated and compared with the available experiments and previous calculations.

2. Computational methodology

Density-functional theory (DFT) calculations were performed using the Vienna *Ab initio* Simulation Package (VASP) [43]. The interaction between valence electrons and ionic cores was described using the projector augmented-wave (PAW) method [44,45]. Exchange–correlation effects were treated within the generalized gradient approximation (GGA) using the Perdew–Burke–Ernzerhof (PBE) functional [46].

Hybrid exchange–correlation functionals are known to improve the description of electronic band gaps compared to semilocal GGA functionals and have been successfully applied to a wide range of oxide materials, yielding good agreement with experimental measurements [47–49]. For this purpose, hybrid-functional calculations were performed using the screened Heyd–Scuseria–Ernzerhof (HSE) functional [50], where 25% of exact Hartree–Fock exchange was included.

The electronic wave functions were expanded in a plane-wave basis set with a kinetic-energy cutoff of 520 eV. Brillouin-zone integrations in reciprocal space were performed using Γ-centered Monkhorst–Pack grids of (9 × 7 × 2), (6 × 6 × 2), and (6 × 6 × 1) k points for the *Imm2* and $Pna2_1$ bulk structures and the surface slab calculations, respectively [51]. Structural relaxations were carried out until the residual forces acting on all atoms were smaller than 0.01 eV/Å, and the electronic self-consistency criterion was set to 10^{-5} eV.

The bulk $Bi_2O_2CO_3$ structures were modeled using periodic repetitions of the orthorhombic unit cell based on experimentally reported crystallographic data [11,12]. Test calculations including semicore Bi-*d* electrons in the valence configuration yielded slightly lower total energies and were therefore adopted in all subsequent calculations.

Because of the heavy atomic mass of Bi, relativistic effects were included by treating spin–orbit coupling (SOC) self-consistently [52]. Long-range dispersion interactions were accounted for using Grimme's DFT-D3 correction scheme [53].

Charge transfer and bonding characteristics were further analyzed through Bader charge analysis and the electron localization function (ELF) [54,55].

Optical properties of the ground-state bulk phase were calculated using the HSE functional. Optical spectra are affected by local-field and electron–hole attraction effects. They are included here by solving the Bethe–Salpeter equation (BSE) [56–58]. For numerical reasons, we use a model dielectric function in the BSE [59,60] and neglect SOC effects in the optical response. In the BSE calculations, 12 valence and 12 conduction bands were included and a Gaussian broadening of 0.05 eV was applied.

Surface properties were investigated using slab geometries derived from the optimized bulk structure. The $Bi_2O_2CO_3$ (001) surface was modeled using periodically repeated slabs with a thickness of approximately 23 Å. A vacuum region of about 32 Å was introduced along the surface normal to avoid spurious interactions between periodic images.

To verify the numerical reliability and physical validity of the surface configuration, systematic convergence tests were carried out for the CO_3-terminated surface by extending the slab thickness from 23 Å to 37 Å. This significant thickness expansion altered the calculated surface free energy by an exceedingly small value of less than 0.24 meV/Å^2, which is well below standard strict convergence thresholds. The largest structural variation observed between the baseline and thicker slab configurations is confined to the terminal C–O bonds, which show a minor deviation of only 0.02 Å. These combined findings definitively confirm that the chosen baseline slab model ensures an excellently converged and physically reliable description of the $Bi_2O_2CO_3$ surface properties.

The slab models were constructed symmetrically in order to eliminate artificial dipole moments perpendicular to the surface. During structural relaxation, atoms near the surface were allowed to relax freely, whereas atoms in the inner layers were constrained to their bulk positions to preserve bulk-like geometry.

The stability of different surface terminations was analyzed using *ab initio* thermodynamics [61–63]. The surface free energy is given by

$$\gamma = \frac{1}{2A}\left(E_{\text{slab}} - \sum_i n_i \mu_i\right), \tag{1}$$

where E_{slab} is the total energy of the slab, A is the surface area, n_i denotes the number of atoms of species i, and μ_i is the corresponding chemical potential. The factor of 2 accounts for the two equivalent surfaces in the symmetric slab model.

The chemical potentials are constrained by thermodynamic equilibrium with bulk $Bi_2O_2CO_3$. Considering Bi bulk as the reference state and O_2 and CO_2 as gas reservoirs, the equilibrium condition can be written as

$$2\mu_{\text{Bi}} + \frac{3}{2}\mu_{\text{O}_2} + \mu_{\text{CO}_2} = \mu^{\text{bulk}}_{\text{Bi}_2\text{O}_2\text{CO}_3} \tag{2}$$

The formation enthalpy of bulk $Bi_2O_2CO_3$ was obtained from DFT total energies as

$$-\Delta H_{f,\text{Bi}_2\text{O}_2\text{CO}_3} = E_{\text{Bi}_2\text{O}_2\text{CO}_3} - \left(2E^{\text{bulk}}_{\text{Bi}} + \frac{3}{2}E^{\text{gas}}_{\text{O}_2} + E^{\text{gas}}_{\text{CO}_2}\right) \tag{3}$$

The chemical potentials are conveniently expressed relative to their reference states using a system of aligned definitions:

$$\Delta\mu_{\text{Bi}} = \mu_{\text{Bi}} - \mu^{\text{bulk}}_{\text{Bi}} \tag{4}$$

$$\Delta\mu_{\text{O}_2} = \mu_{\text{O}_2} - E^{\text{gas}}_{\text{O}_2} \tag{5}$$

$$\Delta\mu_{\text{CO}_2} = \mu_{\text{CO}_2} - E^{\text{gas}}_{\text{CO}_2} \tag{6}$$

Under thermodynamic equilibrium with bulk $Bi_2O_2CO_3$, these chemical potentials satisfy

$$2\Delta\mu_{Bi} + \frac{3}{2}\Delta\mu_{O_2} + \Delta\mu_{CO_2} = \Delta H_{f,Bi_2O_2CO_3} \quad (7)$$

The upper limits $\Delta\mu_{O_2} = 0$ and $\Delta\mu_{CO_2} = 0$ correspond to O_2-rich and CO_2-rich conditions, respectively, while lower limits are determined by the stability of $Bi_2O_2CO_3$ with respect to competing phases. Within the ideal-gas approximation, the temperature and pressure dependence of the gas-phase chemical potentials is given by

$$\Delta\mu_i(T,p) = k_B T \left[\ln\left(\frac{p\lambda_i^3}{k_B T} \right) - \ln Z_i^{rot} - \ln Z_i^{vib} \right] \quad (8)$$

where $i = O_2$ or CO_2, k_B is the Boltzmann constant, and λ_i is the de Broglie thermal wavelength,

$$\lambda = \sqrt{\frac{2\pi\hbar^2}{mk_B T}} \quad (9)$$

while Z_{rot} and Z_{vib} denote the rotational and vibrational partition functions of the molecules.

For the linear molecules O_2 and CO_2, the rotational partition function was evaluated within the high-temperature approximation as [64]

$$Z_{rot} = \frac{T}{\sigma\theta_r} \quad (10)$$

where σ is the symmetry number set to 2 for both O_2 and CO_2, and θ_r is the rotational temperature defined by

$$\theta_r = \frac{hcB}{k_B}, \quad (11)$$

with B being the rotational constant of the O_2 and CO_2 molecules taken from experimental spectroscopic data [65]. The vibrational partition function was computed within the harmonic approximation, including only the thermal vibrational contribution [66]

$$Z_{vib} = \prod_i \frac{1}{1 - \exp\left(-\theta_{v,i}/T\right)}, \quad (12)$$

where $\theta_{v,i} = \frac{hc\nu_i}{k_B}$ is the characteristic vibrational temperature associated with the ith vibrational mode of frequency ν_i. The zero-point energy (ZPE) was added explicitly to the DFT total energy when constructing the 0 K reference for the gas-phase chemical potentials. Surface phase diagrams were constructed as a function of the oxygen and carbon dioxide chemical potentials to identify the thermodynamically stable surface terminations.

3. Results and discussion

3.1. Bulk atomic structure

Two orthorhombic space groups are commonly discussed for $Bi_2O_2CO_3$: *Imm2* (No. 44) and *Pna2*$_1$ (No. 33). The former is conveniently used in computational studies, e.g. Refs. [15,18,67]. Here we perform full structural relaxations for both models using computational settings on the same footing. In either structure, the Bi atoms are coordinated by oxygen atoms belonging both to the oxide layers and to the carbonate units, forming a distorted Bi–O polyhedral environment. For the relaxed *Imm2* structure we determine within DFT-PBE equilibrium lattice constants $a = 3.60$ Å, $b = 4.57$ Å, and $c = 13.91$ Å, as well as nearly uniform C–O bond lengths of about 1.29 Åwithin the carbonate groups. In contrast, the equilibrium *Pna2*$_1$ structure has lattice parameters $a = 5.53$ Å, $b = 5.57$ Å, and $c = 27.90$ Å. The reduced symmetry introduces small distortions in the carbonate units, reflected in slightly different C–O bond lengths of 1.29 and 1.31 Å, and modified O–C–O bond angles. In Fig. 1 both relaxed atomic structures with key structural parameters are shown.

Total-energy calculations show that the *Pna2*$_1$ structure is energetically more stable within DFT-PBE. We calculate an energy difference of 0.265 eV per formula unit. This clearly establishes *Pna2*$_1$ as the thermodynamically preferred structure for bismutite. This is supported by experiment. Powder neutron diffraction [11] determined lattice parameters $a = 5.47$ Å, $b = 5.47$ Å, and $c = 27.32$ Å, close to the DFT-PBE calculation. The slight overestimation in the calculations is expected, as the generalized gradient approximation tends to overestimate lattice constants. Moreover, temperature effects are neglected in the calculations. The thermodynamic preference of the *Pna2*$_1$ phase originates from the additional structural degrees of freedom that become available upon lowering the symmetry relative to the *Imm2* structure. In the *Pna2*$_1$ phase, the carbonate groups undergo slight distortions, as evidenced by the inequivalent C–O bond lengths and deviations from the ideal trigonal O–C–O geometry. These distortions allow a more efficient accommodation of the surrounding Bi-O framework and reduce local strain within the layered structure. Simultaneously, the reduced symmetry enables a stronger expression of the stereochemically active Bi $6s^2$ lone pairs, leading to asymmetric Bi–O coordinations and off-centering of the Bi atoms.

These structural features are consistent with the bonding characteristics obtained from the ELF and Bader charge analysis [54], shown in Fig. 1. The ELF provides a real-space representation of the electronic localization, where high values indicate strongly localized electrons associated with covalent bonding or lone pairs, whereas low values between atoms are characteristic of more ionic or delocalized interactions. In both structures, the ELF maps show pronounced localization around the oxygen atoms and along the C–O bonds, confirming the strong covalent character of the carbonate (CO_3) units. In contrast, the regions between Bi and O atoms exhibit much weaker localization, consistent with the largely ionic nature of the Bi–O bonding network. The Bader charge analysis supports this picture. In the *Pna2*$_1$ structure, Bi atoms carry a charge of about +2.10 *e*, while O atoms exhibit approximately −0.90 *e*, indicating significant charge transfer from Bi toward O. Carbon atoms display a smaller positive charge of roughly +0.40 *e*, consistent with their role in the covalently bonded carbonate groups. A similar bonding motif is obtained for the *Imm2* structure; however, the charge redistribution is somewhat different, with O atoms carrying about −1.11 *e*, Bi atoms about +1.92 *e*, and C atoms approximately +1.73 *e*. Despite the overall similarity of the bonding network, the ELF distribution in the *Pna2*$_1$ structure exhibits slightly stronger localization within the bonding regions of the carbonate units, whereas the *Imm2* structure shows a more diffuse electronic distribution. This difference indicates stronger covalent contributions in the *Pna2*$_1$ structure, consistent with its lower total energy and supporting its identification as the thermodynamically stable ground-state structure.

3.2. Bulk electronic structure

The measured and previously calculated bismutite band gaps scatter broadly. UV–Vis data by Zheng et al. [23] were interpreted in terms of a 3.1 eV band gap. Sponge-like, rose-like and plate-like bismutite samples were measured to have band gaps of 2.9, 3.0, and 3.3 eV, respectively [68]. A band gap of 3.4 eV has been determined by Huang and co-workers [12]. These measured values are considerably larger than the DFT values of 0.8 eV and 2.30 eV calculated by Reshak and Auluck [15] and Guan et al. [18], respectively. While the apparent underestimation of the measured band gap in the latter case may be attributed to the DFT band gap problem, the calculated value of 0.8 eV seems hard to reconcile with experiment. It has to be said, however, that both calculated values were obtained assuming *Imm2* symmetry.

Here the bismutite electronic properties are investigated for both *Pna2*$_1$ and *Imm2* structures. Owing to the presence of heavy Bi atoms, relativistic effects are expected to be noticeable in the electronic band structure, especially for states near the band edges. Therefore, the band

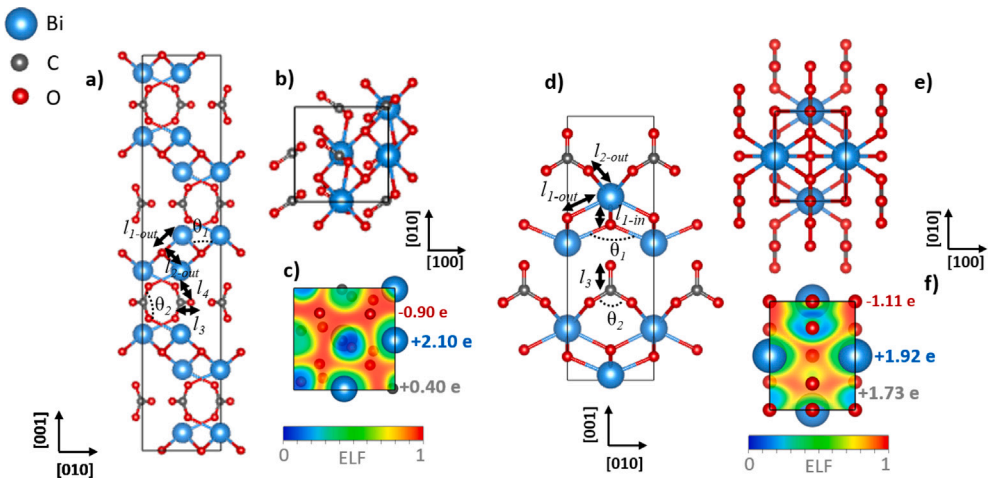

Fig. 1. Relaxed bismutite atomic structures assuming *Pna2*$_1$ and *Imm2* symmetry. (a,d) Top views and (b,e) side views, respectively, showing the most relevant bond lengths and bond angles. Respective values of 2.32 Å, 2.55 Å, 2.54 Å, 1.29 Å, 62.95°, and 118.55° are calculated for $l_{1\text{-in}}$, $l_{1\text{-out}}$, $l_{2\text{-out}}$, l_3, θ_1, and θ_2 in *Pna2*$_1$ symmetry. For *Imm2* we calculate 2.39 Å, 2.32 Å, 1.29 Å, 1.31 Å, 56.81°, and 120.59° respectively for $l_{1\text{-out}}$, $l_{2\text{-out}}$, l_3, l_4, θ_1, and θ_2. Bottom panels present the average Bader charge transfer and 2D ELF contour maps for both structures. The color scheme used here is also applied in the subsequent figures.

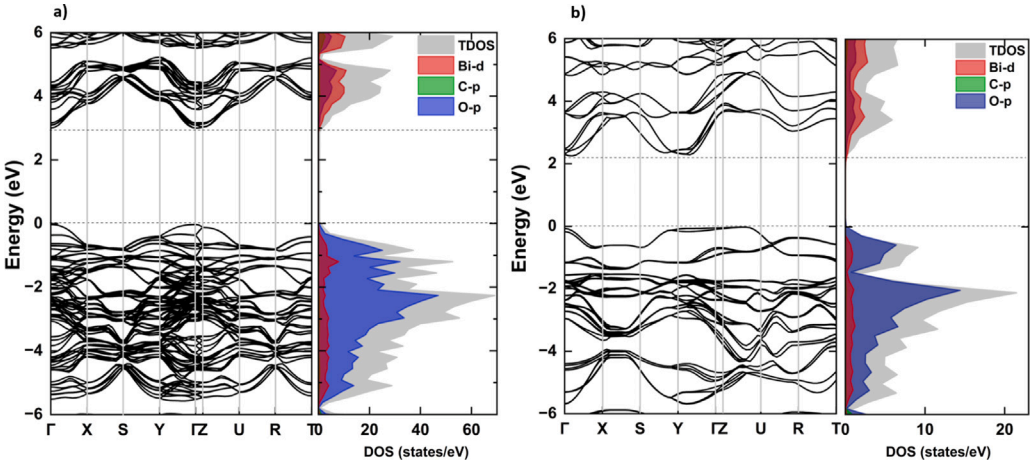

Fig. 2. Band structures and orbital-resolved densities of states of $Bi_2O_2CO_3$ calculated within the HSE06+SOC approach for the (a) *Pna2*$_1$ and (b) *Imm2* structures. The band gap is indicated by dotted lines, and energies are referenced to the valence-band maximum.

Table 1
Calculated bismutite band gaps and lowest energy transitions in the Brillouin zone.

Structure	Method	Band gap (eV)	Transition
Imm2	PBE	1.10 (id)	ZU → YΓ
	PBE+SOC	0.70 (id)	ZU → Γ
	HSE+SOC	2.27 (id)	ZU → Γ
Pna2$_1$	PBE	2.14 (d)	Γ → Γ
	PBE+SOC	1.77 (id)	Γ → ΓZ
	HSE+SOC	3.03 (d)	Γ → Γ

structures were evaluated at the PBE, PBE+SOC, and HSE06+SOC level of theory.

The calculated band structures together with the total and projected densities of states (TDOS and PDOS) obtained within the HSE06+SOC approach are shown in Fig. 2, and the band-gap values for all computational schemes are summarized in Table 1. At the PBE level, the *Pna2*$_1$ structure exhibits a direct band gap of 2.14 eV. The inclusion of SOC leads to a pronounced modification of the band dispersion, reducing the gap to 1.77 eV and inducing a transition from direct to indirect. A similar trend is observed for the *Imm2* structure, where the band gap decreases from 1.10 to 0.70 eV upon inclusion of SOC. This behavior reflects the strong spin–orbit interaction of Bi-derived states, which lifts band degeneracies near the band edges and shifts the relative position of the conduction-band minimum across k-space.

A more reliable description is obtained within the HSE06+SOC framework. In this case, the *Pna2*$_1$ structure is found to be a direct-gap semiconductor with a band gap of 3.03 eV, whereas the *Imm2* structure exhibits an indirect gap of 2.27 eV. The difference in band-gap magnitude between the two structures can be attributed to the symmetry lowering in the *Pna2*$_1$ structure, which modifies the orbital overlap and leads to a stronger separation between valence and conduction states. The calculated gap for the *Pna2*$_1$ structure of about 3 eV is in excellent agreement with the experimental values ranging from 2.9 ⋯ 3.4 eV [12,23,68], while the HSE+SOC value of about 2.3 eV for the *Imm2* structure is clearly outside the measured range. We further note that experimental studies report a direct band gap, [69] in agreement with our HSE+SOC results for the *Pna2*$_1$ phase, whereas indirect gaps reported in the literature are predominantly associated with calculations based on the *Imm2* structure. This consistency between the calculated direct gap and experiment provides additional support for identifying *Pna2*$_1$ as the correct bismutite ground-state.

Further insight into the electronic structure is obtained from the orbital-resolved densities of states shown in Fig. 2. In both structures,

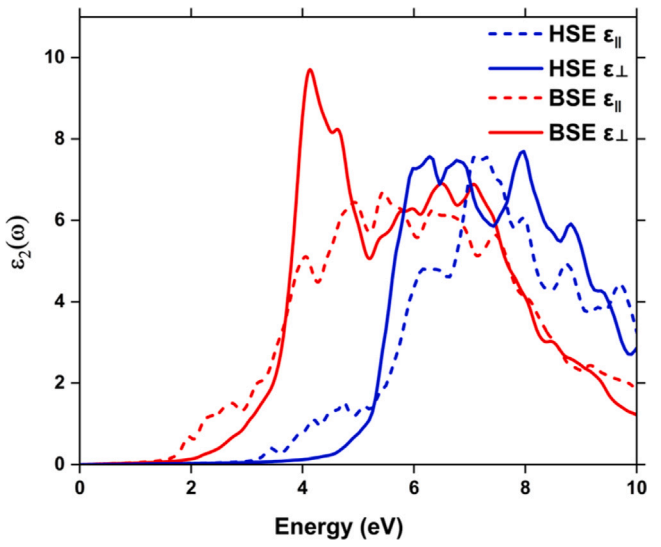

Fig. 3. Imaginary parts of the dielectric function for the $Pna2_1$ phase of bismutite calculated on the HSE and HSE+BSE levels of theory. Here $\varepsilon\|$ is obtained by averaging the in-plane components of the dielectric tensor, whereas $\varepsilon_\perp$ corresponds to the [001] direction.

the valence-band maximum (VBM) is dominated by O-*p* states, while the conduction-band minimum (CBM) is primarily composed of Bi-derived states, with additional contributions from O-*p* orbitals. The contribution of C states near the band edges is comparatively small. The overlap between Bi and O states in the same energy range indicates significant hybridization, which governs the nature of the band edges and is consistent with the mixed ionic–covalent bonding character discussed above.

Concerning the comparison of measured and calculated band gaps in Table 1, a word of caution is in order. The experimental band gaps are derived from optical spectroscopy and may thus be affected by excitonic effects.

To assess their influence, HSE optical response calculations for the *Pna2*1 phase were performed, both with and without excitonic effects, the latter included by solving the BSE. The resulting imaginary parts of the dielectric function, $\varepsilon_2(\omega)$, are shown in Fig. 3. The optical response of bismutite is strongly anisotropic. The onset of absorption is dominated by in-plane components, whereas the strongest absorption peak arises from $\varepsilon_\perp$. This anisotropy may account for the pronounced deviations between the measured absorbance of different bismutite samples reported by Zheng et al. [23]. The inclusion of electron–hole interactions leads to a redistribution of spectral weight toward lower energies. In particular, the absorption peak associated with $\varepsilon_\perp$ is sharpened and red-shifted. Clearly, the reduced dielectric screening and the structural anisotropy of the layered bismuth-oxide framework give rise to strong and anisotropic excitonic effects that hinder a direct interpretation of UV–Vis spectra in terms of single-particle bands.

3.3. Surface structure and thermodynamic stability

The (001) surface of $Bi_2O_2CO_3$ is the dominant facet, a feature attributed to the layered stacking of alternating $[Bi_2O_2]^{2+}$ and $[CO_3]^{2-}$ units along the *c* axis [36,42]. This structural motif naturally promotes oxygen-rich terminations upon cleavage [22]. Within the bulk $Pna2_1$ structure, the Bi–O coordination exhibits a pronounced anisotropy, with elongated out-of-plane bonds ($l_{1\text{-out}}$ = 2.39 Å and $l_{2\text{-out}}$ = 2.32 Å, see Fig. 1), defining the preferential cleavage planes and driving the subsequent surface relaxation.

Here four surface termination models-denoted as T_1 (CO_2 terminated), T_2 (Bi terminated), T_3 (O terminated), and T_4 (Bi_2O_2 terminated) are considered. They result from $Pna2_1$ bulk by successive layer removal. The surface structures, shown in Fig. 4 were fully relaxed to account for the coordination changes and stereochemical activity of the Bi $6s^2$ lone pairs at the vacuum interface. Upon relaxation, the surface layers exhibit significant atomic displacements relative to the bulk structure, with variations depending on the termination. For T_1, the atoms exhibit relatively small displacements of approximately 0.10–0.35 Å. The configuration thus remains close to the ideal bulk truncation, characterized by only slight rotations of the CO_3 groups. A marginally larger relaxation is observed for T_2, where surface Bi and C atoms exhibit the highest mobility with displacements reaching up to 0.40 Å, suggesting a weak surface rearrangement and CO_3 rotation while still preserving a largely bulk-like geometry. In contrast, T_3 shows significantly enhanced relaxation along the surface normal, with typical displacements ranging from 0.25 to 0.50 Å. This structural response is primarily driven by the outermost Bi atoms, which shift to accommodate the additional oxygen species and the associated modification of the local bonding environment; notably, unlike T_1 and T_2, the CO_3 units in T_3 exhibit negligible rotation, with oxygen atoms contributing most significantly to the observed surface disorder. The largest distortions occur in T_4, where the atomic displacements reach 0.35–0.60 Å. This pronounced surface relaxation is driven by the tilting of oxygen atoms to satisfy the altered Bi coordination at the surface.

The structural relaxation was further quantified by evaluating the evolution of key bond lengths and angles relative to their bulk counterparts. The $[CO_3]^{2-}$ groups exhibit high structural rigidity, with C–O bond lengths deviating by only 2.3% to 3.8% (1.24–1.32 Å) from the bulk 1.29 Å. This internal stability is further reflected in the internal C–O–O bond angles (θ_2), which deviate from the bulk 120.59° to a range of 79.0°–121.0°. This spread indicates that the structural response is largely governed by collective tilting of the carbonate units, although noticeable internal angular distortions are also present.

Conversely, the Bi–O–O bond angle (θ_1) remains remarkably stable, shifting from 56.81° in the bulk to only 57.49° after relaxation. In contrast, the Bi–O coordination environment shows significantly larger deviations governed by local stoichiometry and symmetry breaking. The out-of-plane Bi-O bonds ($l_{1\text{-out}}$ = 2.39 Å) shift by up to 5.4% (2.26–2.41 Å), while the second set of out-of-plane bonds ($l_{2\text{-out}}$ = 2.32 Å) exhibits a pronounced redistribution spanning 2.06 to 2.58 Å. This 11.2% deviation reflects substantial local rearrangements where stereochemical $6s^2$ lone-pair activity is most prominent.

To our knowledge, there are no previous first-principles calculations addressing the structures and stabilities of $Bi_2O_2CO_3$ surfaces. Nevertheless, the properties and bonding characteristics calculated here are consistent with previous findings for Bi-related surfaces [70–72]. Specifically, the exceptionally rigid nature of the internal $[Bi_2O_2]^{2+}$ network preserved in our slab core confirms the behavior of the oxide layer acting as an unperturbed structural unit, directly matching the BiOX block stability observed by Cabeza et al. [72]. To accommodate the broken covalent bonds and the resulting "electron spilling" at the vacuum boundary highlighted by Huang et al. [70], the outermost surface skin undergoes a localized symmetry break. This distortion is mostly absorbed by the terminal carbonate groups. Because this geometry relaxation is highly confined to the outer layer, the interior core rapidly recovers bulk-like properties. This localized screening mechanism mirrors the thickness-dependent protection found in non-van der Waals Bi_2O_2X blocks [71]. The strong confinement of the surface relaxation to the outermost surface layers is also proven by the very minor changes of the surface properties upon slab expansion as discussed in the method section.

The relative thermodynamic stability of the four terminations $T_1 \cdots T_4$ is evaluated by calculating the surface phase diagram in dependence on the oxygen and carbon dioxide chemical potentials, see Fig. 5. A clear hierarchy of stability emerges. The T_1 termination

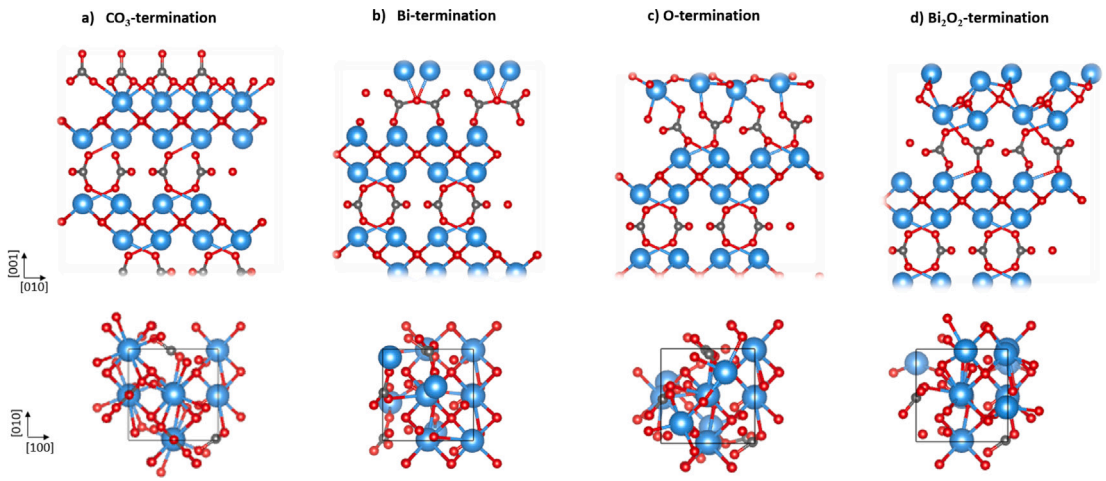

Fig. 4. Side and top views of the four relaxed (001) surface terminations of $Pna2_1$-$Bi_2O_2CO_3$: (a) T1 (CO_2-term), (b) T2 (Bi-term), (c) T3 (O-term), and (d) T4 (Bi_2O_2-term). The crystallographic directions are indicated.

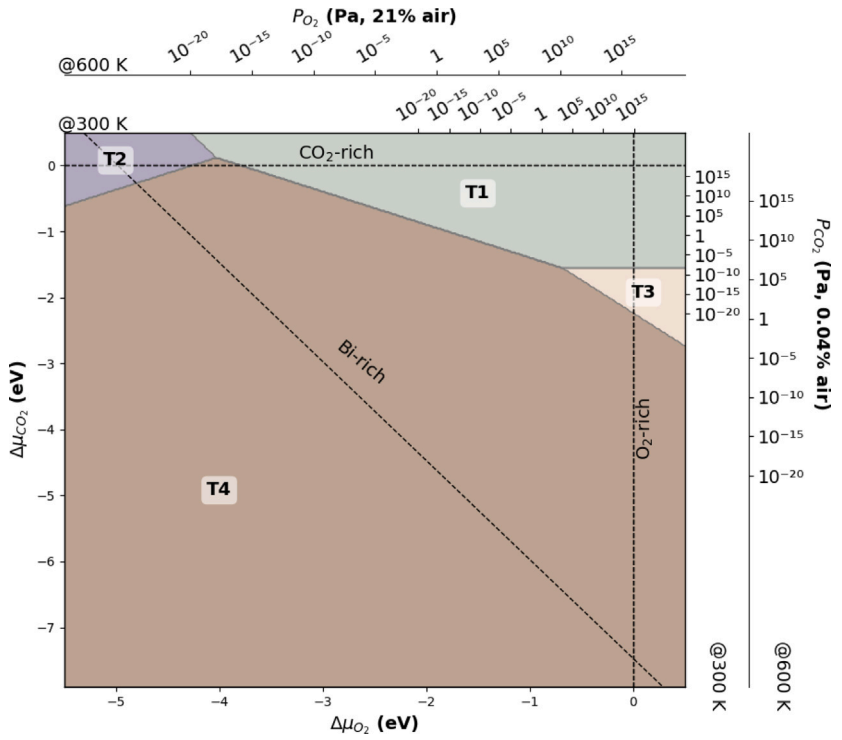

Fig. 5. Surface phase diagram of the (001) facet of $Bi_2O_2CO_3$, showing the stability regions of the four surface terminations (T_1–T_4) as a function of the oxygen and carbon dioxide chemical potentials, $\Delta\mu_{O_2}$ and $\Delta\mu_{CO_2}$. The thermodynamically allowed range, as defined by Eqs. (4) and (5), is indicated by dashed lines. The shaded regions denote representative experimental conditions, with the upper-right region corresponding to ambient conditions and the lower-left region to ultra-high vacuum (UHV). The top and right axes show the corresponding partial pressures at T = 300 and 600 K.

occupies a broad range of the phase diagram corresponding to ambient conditions. T_1 thus represents in many instances the most likely observed termination. In contrast, T_2 is stable only in a very narrow region characterized by CO_2-rich and O_2-poor conditions. Similarly, T_3 is favorable in a small region of the phase diagram characterized by under oxygen-rich conditions. T_4, finally, is stable for wide range of preparations conditions characterized by low pressure. Interestingly, however, ultrahigh vacuum conditions are outside the stability range of the phase diagram. This agrees with the experimental finding that high temperatures (or low pressures) destabilize bismutite [11,34,35].

3.4. Surface electronic structure

In Fig. 6, the $T_1 \cdots T_4$ surface electronic bands calculated within DFT-PBE within the bismutite bulk band region are shown together with the surface projected bulk band structure. In addition, the orbital character of the corresponding states at selected k points is shown by evaluating their squared wavefunctions.

For T_1, the bulk band gap is essentially free of states. There are no bound surface states apart from a weakly dispersive band close to the bulk valence-band maximum (VBM). The corresponding wavefunction

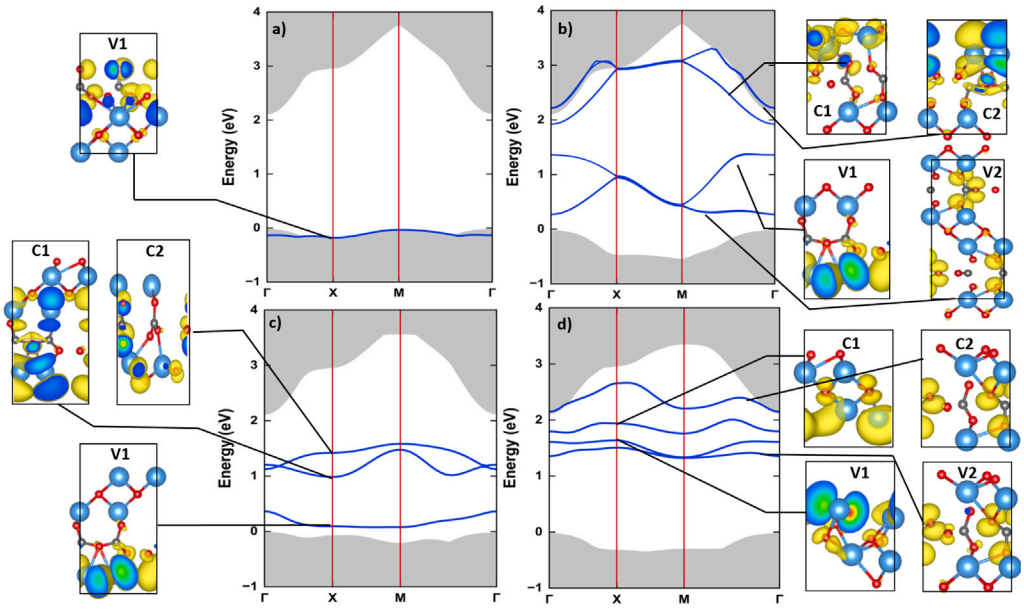

Fig. 6. (a–d) Projected surface band structures of the four terminations ($T_1 - T_4$) of $Bi_2O_2CO_3$ (001) (blue solid lines), superimposed on the projected bulk band structure of the *Pna2*$_1$ structure (light gray shading). Energies are referenced to the valence-band maximum of the bulk. Left and right panels show the corresponding squared wavefunctions at the X point, illustrating the surface states V1 and V2 in the valence band and C1 and C2 in the conduction band.

is localized at the surface oxygen atoms. The electronic passivated character of T_1 is in line with its thermodynamic stability. In contrast, T_2 shows a Fermi-level pinning by surface states in the upper part of the band gap. The empty surface states *C1* and *C2* lie slightly below the bulk conduction-band minimum (CBM). These states are localized at surface Bi atoms. In the lower half of the band gap, there are occupied surface states *V1* and *V2* that show strong localization on surface oxygen atoms, with only minor contributions from Bi orbitals. In case of T_3, the Fermi level is pinned by surface states in the lower half of the band gap. The surface state *V1* is located close to the VBM and arises primarily from subsurface oxygen atoms within carbonate groups and exhibits a predominantly nonbonding O-*p* character, with a minor contribution from Bi orbitals. In addition, unoccupied surface states related primarily to empty Bi states appear within the gap at about 1 eV below the CBM. A higher density of surface states within the band gap is also found for T_4. Surface Bi-related states and subsurface O states pin the Fermi level below the bulk CBM.

For all terminations, the ELF (not shown here) shows strong localization around the oxygen atoms and along the C–O bonds, confirming the covalent character of the carbonate groups, whereas the weaker localization between Bi and O reflects the ionic nature of the Bi–O framework. Differences between terminations arise mainly in the spatial distribution of the ELF near the surface: T_1 exhibits a charge density largely confined within the slab, whereas T_2 shows a more diffuse distribution extending toward the vacuum region. The T_3 termination displays non-uniform localization indicative of charge polarization, while T_4 presents a strongly heterogeneous distribution associated with significant surface reconstruction. This behavior is supported by the Bader charge analysis. For T_1, the charges remain close to bulk values, with Bi (+2.0–+2.2 *e*), O (−0.8 to −1.0 *e*), and C (+0.3–+0.5 *e*), confirming minimal surface-induced charge transfer. In contrast, T_2 exhibits a broader charge distribution, with more negatively charged oxygen (down to ∼−1.2 *e*) and variations in Bi and C charges, indicating a distortion of the carbonate units. T_3 shows intermediate behavior with noticeable charge polarization across the slab, while T_4 exhibits the highest deviations (Bi (+1.6–+2.1 *e*), O (−0.6 to −1.0 *e*), and C (up to ∼ + 1.0 *e*)), with strongly inhomogeneous charge states reflecting pronounced rearrangement.

4. Summary

We present a comprehensive density-functional theory study of the bulk and (001) surface properties of bismutite ($Bi_2O_2CO_3$). A systematic comparison of the commonly assumed *Imm2* structure with the lower-symmetry *Pna2*$_1$ phase reveals the latter to be energetically favored and in better agreement with experimental observations. This structural refinement leads to a significantly larger band gap, with hybrid-functional calculations including spin–orbit coupling (SOC) yielding a value of about 3 eV, consistent with available measurements. The electronic structure is found to be strongly influenced by SOC effects, which modify band dispersion and gap character. In addition, excitonic effects are show to affect strongly the bismutite optical response. Surface properties are investigated using *ab initio* thermodynamics, identifying a CO_3-terminated (001) surface as the thermodynamically stable configuration under ambient conditions. This termination exhibits an electronically passivated character with no significant surface states within the bulk band gap. In contrast, alternative terminations stabilized under non-ambient conditions introduce pronounced surface states that pin the Fermi level within the gap. These states originate from undercoordinated Bi and O atoms and reflect substantial surface relaxation. The results provide a consistent microscopic picture of the interplay between structure, stability, and electronic properties in $Bi_2O_2CO_3$, and offer guidance for tailoring its surface-dependent behavior in catalytic and photoactive applications.

CRediT authorship contribution statement

W. Elaggoune: Writing – original draft, Visualization, Software, Investigation, Formal analysis, Data curation. **I.A. Ruiz Alvarado:** Writing – review & editing, Visualization, Validation, Software, Data curation. **G. Grundmeier:** Writing – review & editing, Visualization, Validation, Investigation. **W.G. Schmidt:** Writing – review & editing, Validation, Supervision, Resources, Project administration, Formal analysis, Conceptualization.

Declaration of competing interest

The authors declare that they have no known competing financial interests or personal relationships that could have appeared to influence the work reported in this paper.

Acknowledgments

The DFG, Germany (SCHM1361/35) is gratefully acknowledged for financial support. We thank the Paderborn Center for Parallel Computing (PC^2) for grants of high-performance computer time.

Data availability

Data will be made available on request.

References

[1] S. Andersson, A. Åstrom, The stereochemistry of the inert pair in some solid oxides or oxide fluorides of Sb^{3+}, Bi^{3+} and Pb^{2+}, in: Solid State Chemistry–Proceedings of the 5th Materials Research Symposium, National Bureau of Standards Special Publication, Vol. 364, 1972, pp. 3–14.

[2] A. Al-Sharabi, K.S. Sada'a, A. Al-Osta, R. Abd-Shukor, Structure, optical properties and antimicrobial activities of MgO–$Bi_{2-x}Cr_xO_3$ nanocomposites prepared via solvent-deficient method, Sci. Rep. 12 (1) (2022) 10647.

[3] H.-Y. Deng, W.-C. Hao, H.-Z. Xu, A transition phase in the transformation from α-, β-and-to δ-Bismuth Oxide, Chin. Phys. Lett. 28 (5) (2011) 056101.

[4] L.G. Sillén, Über eine familie von oxyhalogeniden, Naturwissenschaften 30 (22) (1942) 318–324.

[5] J.-Y. Kim, I. Chung, J.-H. Choy, G.-S. Park, Macromolecular nanoplatelet of aurivillius-type layered perovskite oxide, $Bi_4Ti_3O_{12}$, Chem. Mater. 13 (9) (2001) 2759–2761.

[6] Y. Tsunoda, W. Sugimoto, Y. Sugahara, Intercalation behavior of n-alkylamines into a protonated form of a layered perovskite derived from aurivillius phase $Bi_2SrTa_2O_9$, Chem. Mater. 15 (3) (2003) 632–635.

[7] K. Aurivillius, B. Malmros, Studies on sulfates, selenates and chromates of mercury (II), Acta Chem. Scand. 15 (1961) 1932.

[8] R. Turcotte, J. Sawyer, L. Eyring, Inorg. Chem. 8 (1969) 238.

[9] D. Charkin, P. Berdonosov, A. Moisejev, R. Shagiakhmetov, V. Dolgikh, P. Lightfoot, A novel family of layered bismuth compounds: I. The crystal structures of $Pb_{0.6}Bi_{1.4}Cs_{0.6}O_2Cl_2$ and $Pb_{0.6}Bi_{3.4}Cs_{0.6}O_4Cl_4$, J. Solid State Chem. 147 (2) (1999) 527–535.

[10] J.D. Grice, A solution to the crystal structures of bismutite and beyerite, Can. Miner. 40 (2) (2002) 693–698.

[11] C. Greaves, S. Blower, Structural relationships between $Bi_2O_2CO_3$ and β-Bi_2O_3, Mater. Res. Bull. 23 (7) (1988) 1001–1008.

[12] H. Huang, N. Tian, S. Jin, Y. Zhang, S. Wang, Syntheses, characterization and nonlinear optical properties of a bismuth subcarbonate $Bi_2O_2CO_3$, Solid State Sci. 30 (2014) 1–5.

[13] Z. Ni, Y. Sun, Y. Zhang, F. Dong, Fabrication, modification and application of $(BiO)_2CO_3$-based photocatalysts: a review, Appl. Surf. Sci. 365 (2016) 314–335.

[14] R. More, M. Olah, S.E. Balaghi, P. Jaker, S. Siol, Y. Zhou, G.R. Patzke, $Bi_2O_2CO_3$ growth at room temperature: in situ X-ray diffraction monitoring and thermal behavior, ACS Omega 2 (11) (2017) 8213–8221.

[15] A. Reshak, S. Auluck, Dispersion of the linear and nonlinear optical susceptibilities of bismuth subcarbonate $Bi_2O_2CO_3$: DFT calculations, Opt. Mater. 38 (2014) 80–86.

[16] Y. Liu, Z. Wang, B. Huang, K. Yang, X. Zhang, X. Qin, Y. Dai, Preparation, electronic structure, and photocatalytic properties of $Bi_2O_2CO_3$ nanosheet, Appl. Surf. Sci. 257 (1) (2010) 172–175.

[17] C. Zhu, Q. Liu, H. Yan, W. Zhang, R. Chen, Sulfur-doped $Bi_2O_2CO_3$ nanosheet for enhanced visible-light-driven photocatalytic CO_2 reduction to CO with ultra-high selectivity, Chem. Sustain. Chem. 18 (2) (2025) e202401054.

[18] T. Guan, K. Gong, Z. Shi, B. Chen, K. Xie, M. Gao, K. Huang, Y. Mao, X. Liu, J. Wu, et al., Doping with iodine to modulate the band gap and oxygen vacancy concentration of $Bi_2O_2CO_3$ to enhance the photocatalytic oxidation of Hg0, J. Environ. Chem. Eng. 13 (2) (2025) 115948.

[19] X. Sun, G. Liu, R. Li, L. Li, J. Dai, H. Yang, Experimental and theoretical revealing of piezo-photocatalyst $Bi_2O_2CO_3$ for degradation of ciprofloxacin in water, Environ. Sci. Pollut. Res. 31 (5) (2024) 7194–7213.

[20] L. Li, X. Sun, T. Xian, H. Gao, S. Wang, Z. Yi, X. Wu, H. Yang, Template-free synthesis of $Bi_2O_2CO_3$ hierarchical nanotubes self-assembled from ordered nanoplates for promising photocatalytic applications, Phys. Chem. Chem. Phys. 24 (14) (2022) 8279–8295.

[21] X. Qiu, X. Sun, J. Ma, Z. Yi, G. Liu, J. Dai, H. Yang, $Bi_2O_2CO_3$-coating on beverage-derived carbon microspheres to achieve highly-efficient photocatalysts for ciprofloxacin degradation, J. Alloys Compd. 970 (2024) 172608.

[22] L.-M. Yang, G.-Y. Zhang, H.-R. Wang, X. Bai, X.-Q. Shen, J.-W. Liu, D.-Z. Gao, Mild synthesis of {001} facet predominated $Bi_2O_2CO_3$ clusters with outstanding simulated sunlight photocatalytic activities, Cryst.Eng.Comm. 18 (20) (2016) 3683–3695.

[23] Y. Zheng, F. Duan, M. Chen, Y. Xie, Synthetic $Bi_2O_2CO_3$ nanostructures: novel photocatalyst with controlled special surface exposed, J. Mol. Catal. A Chem. 317 (1–2) (2010) 34–40.

[24] L. Chen, R. Huang, S.-F. Yin, S.-L. Luo, C.-T. Au, Flower-like $Bi_2O_2CO_3$: Facile synthesis and their photocatalytic application in treatment of dye-containing wastewater, Chem. Eng. J. 193 (2012) 123–130.

[25] E. Luévano-Hipólito, L. Torres-Martínez, M. Vega-Mendoza, M.Z. Treviño-Garza, J.M. Vázquez-Guillén, J.G.B. Gonzalez, C. Rodríguez-Padilla, Photocatalytic performance of alkali-activated materials functionalized with β-Bi_2O_3/$Bi_2O_2CO_3$ heterostructures for environmental remediation, Constr. Build. Mater. 320 (2022) 126205.

[26] L. Zhou, X. Liu, Y. Pang, Y. Luo, H. Lou, D. Yang, X. Qiu, Energy level mediation of $Bi_2O_2CO_3$ cooperates with the noble metal-like catalysis of bi for enhancing the photodegradation activity of organic pollutants, Sep. Purif. Technol. 319 (2023) 124099.

[27] L. Meng, L. Chang, J. Hou, Degradation of methyl green from wastewater with ultrasound synergized with $Bi_2O_2CO_3$ catalysis: Kinetics, products, and pathways, J. Clean. Prod. 342 (2022) 130976.

[28] H. Huang, X. Li, J. Wang, F. Dong, P.K. Chu, T. Zhang, Y. Zhang, Anionic group self-doping as a promising strategy: band-gap engineering and multi-functional applications of high-performance CO_3-doped-$Bi_2O_2CO_3$, ACS Catal. 5 (7) (2015) 4094–4103.

[29] Y. Xiao, X. Lai, J. Feng, Z. Feng, W. Zhang, L. Li, W.F. Ip, H. Pan, Self-refreshing Bi-based active sites for efficient and durable electrochemical CO_2 reduction, Adv. Funct. Mater. 36 (27) (2026) e23592.

[30] Y. Xiao, D. Liu, J. Yang, J. Feng, W. Gu, L. Qiao, W.F. Ip, H. Pan, Controllable reconstruction of β-Bi_2O_3/$Bi_2O_2CO_3$ composite for highly efficient and durable electrochemical CO_2 conversion, Nano Lett. 25 (16) (2025) 6548–6555.

[31] L.G. Puppin, M. Khalid, G.T. da Silva, C. Ribeiro, H. Varela, O.F. Lopes, Electrochemical reduction of CO_2 to formic acid on $Bi_2O_2CO_3$/carbon fiber electrodes, J. Mater. Res. 35 (3) (2020) 272–280.

[32] C.F. Guo, J. Zhang, Y. Tian, Q. Liu, A general strategy to superstructured networks and nested self-similar networks of bismuth compounds, ACS Nano 6 (10) (2012) 8746–8752.

[33] Y. Zhou, H. Wang, M. Sheng, Q. Zhang, Z. Zhao, Y. Lin, H. Liu, G.R. Patzke, Environmentally friendly room temperature synthesis and humidity sensing applications of nanostructured $Bi_2O_2CO_3$, SSens. Actuators B Chem. 188 (2013) 1312–1318.

[34] E.M. Levin, R.S. Roth, Polymorphism of bismuth sesquioxide. I. Pure Bi_2O_3, J. Res. Natl. Bur. Stand. Sect. A Phys. Chem. 68 (2) (1964) 189.

[35] S. Blower, C. Greaves, The structure of β-Bi_2O_3 from powder neutron diffraction data, Cryst. Struct. Commun. 44 (4) (1988) 587–589.

[36] H. Huang, J. Wang, F. Dong, Y. Guo, N. Tian, Y. Zhang, T. Zhang, Highly efficient $Bi_2O_2CO_3$ single-crystal lamellas with dominantly exposed {001} facets, Cryst. Growth Des. 15 (2) (2015) 534–537.

[37] X. Yang, Y. Wang, N. He, W. Wan, F. Zhang, B. Zhai, P. Zhang, One-step hydrothermal synthesis of hierarchical nanosheet-assembled $Bi_2O_2CO_3$ microflowers with a {001} dominant facet and their superior photocatalytic performance, Nanotechnology 31 (37) (2020) 375604.

[38] Y. Yang, Z. Yang, Z. Lai, C. Yang, Y. Hou, H. Tao, J. Zhang, M. Anpo, X. Fu, Crystal facet engineering of $Bi_2O_2CO_3$ nanosheets to enhance photocatalytic ozonation: Unraveling ozone adsorption and electron transfer mechanism, Chin. J. Catal. 72 (2025) 143–153.

[39] X. Su, D. Wu, Controllable synthesis of plate BiOBr loaded plate $Bi_2O_2CO_3$ with exposed {001} facets for ciprofloxacin photo-degradation, J. Ind. Eng. Chem. 64 (2018) 256–265.

[40] L. Cheng, X. Hu, L. Hao, Template-induced $Bi_2O_2CO_3$ microstructure self-assembled by nanosheets with exposed {001} facets, Mater. Res. Express 5 (6) (2018) 065901.

[41] H. Liu, M. Luo, J. Hu, T. Zhou, R. Chen, J. Li, β-Bi_2O_3 and Er^{3+} doped β-Bi_2O_3 single crystalline nanosheets with exposed reactive {001} facets and enhanced photocatalytic performance, Appl. Catal. B Environ. 140 (2013) 141–150.

[42] F. Wang, Z. Zhao, K. Zhang, F. Dong, Y. Zhou, Topochemical transformation of low-energy crystal facets to high-energy facets: a case from $Bi_2O_2CO_3$ {001} facets to β-Bi_2O_3 {001} facets with improved photocatalytic oxidation of NO, Cryst.Eng.Comm. 17 (32) (2015) 6098–6102.

[43] G. Kresse, J. Furthmüller, Efficiency of ab-initio total energy calculations for metals and semiconductors using a plane-wave basis set, Comput. Mater. Sci. 6 (1) (1996) 15–50.

[44] P.E. Blöchl, Projector augmented-wave method, Phys. Rev. B 50 (24) (1994) 17953.

[45] G. Kresse, D. Joubert, From ultrasoft pseudopotentials to the projector augmented-wave method, Phys. Rev. B 59 (3) (1999) 1758.

[46] J.P. Perdew, K. Burke, M. Ernzerhof, Generalized gradient approximation made simple, Phys. Rev. Lett. 77 (18) (1996) 3865.

[47] R.I. Eglitis, R. Jia, Review of systematic tendencies in (001),(011) and (111) surfaces using B3PW as well as B3LYP computations of $BaTiO_3$, $CaTiO_3$, $PbTiO_3$, $SrTiO_3$, $BaZrO_3$, $CaZrO_3$, $PbZrO_3$ and $SrZrO_3$ perovskites, Materials 16 (24) (2023) 7623.

[48] R.I. Eglitis, J. Purans, R. Jia, S.P. Kruchinin, S. Wirth, Comparative B3PW and B3LYP calculations of ABO_3 (A=Ba, Sr, Pb, Ca; B=Sn, Ti, Zr) neutral (001) and polar (111) surfaces, Inorganics 13 (4) (2025) 100.
[49] R.I. Eglitis, J. Purans, A.I. Popov, R. Jia, S.P. Kruchinin, B3PW and B3LYP simulations of ABO_3 perovskite (001) surfaces, interfaces, and oxygen vacancies therein, Symmetry 18 (4) (2026) 550.
[50] J. Heyd, G.E. Scuseria, M. Ernzerhof, Hybrid functionals based on a screened Coulomb potential, J. Chem. Phys. 118 (18) (2003) 8207–8215.
[51] H.J. Monkhorst, J.D. Pack, Special points for Brillouin-zone integrations, Phys. Rev. B 13 (12) (1976) 5188.
[52] Y.M. Koroteev, G. Bihlmayer, J. Gayone, E.V. Chulkov, S. Blügel, P.M. Echenique, P. Hofmann, Strong spin-orbit splitting on Bi surfaces, Phys. Rev. Lett. 93 (4) (2004) 046403.
[53] S. Grimme, J. Antony, S. Ehrlich, H. Krieg, A consistent and accurate ab-initio parametrization of density functional dispersion correction (DFT-D) for the 94 elements H-Pu, J. Chem. Phys. 132 (15) (2010).
[54] R.F. Bader, Atoms in molecules, Acc. Chem. Res. 18 (1) (1985) 9–15.
[55] W. Elaggoune, Ab-Initio Study of the Properties of the 3D SrS-based Mono-Doped and Co-Doped Compounds. A Comparative Study of the 2D and 3D Mono-Doped Compounds (Ph.D. thesis), 2024.
[56] S. Albrecht, L. Reining, R. Del Sole, G. Onida, Ab initio calculation of excitonic effects in the optical spectra of semiconductors, Phys. Rev. Lett. 80 (1998) 4510–4513.
[57] M. Rohlfing, S.G. Louie, Electron-hole excitations in semiconductors and insulators, Phys. Rev. Lett. 81 (1998) 2312–2315.
[58] W.G. Schmidt, S. Glutsch, P.H. Hahn, F. Bechstedt, Efficient $\mathcal{O}(N^2)$ method to solve the Bethe-Salpeter equation, Phys. Rev. B 67 (2003) 085307.
[59] F. Bechstedt, R. Del Sole, G. Cappellini, L. Reining, An efficient method for calculating quasiparticle energies in semiconductors, Solid State Commun. (ISSN: 0038-1098) 84 (7) (1992) 765–770.
[60] P. Liu, B. Kim, X.-Q. Chen, D.D. Sarma, G. Kresse, C. Franchini, Relativistic GW+BSE study of the optical properties of Ruddlesden-Popper iridates, Phys. Rev. Mater. 2 (2018) 075003.
[61] G.-X. Qian, R.M. Martin, D. Chadi, Stoichiometry and surface reconstruction: An ab initio study of GaAs (100) surfaces, Phys. Rev. Lett. 60 (19) (1988) 1962.
[62] K. Reuter, C. Stampf, M. Scheffler, Ab initio atomistic thermodynamics and statistical mechanics of surface properties and functions, in: Handbook of Materials Modeling: Methods, Springer, 2005, pp. 149–194.
[63] W. Schmidt, (4× 2) and (2× 4) reconstructions of GaAs and InP (001) surfaces, Appl. Phys. A Mater. Sci. Process. 65 (6) (1997).
[64] R.S. McDowell, Rotational partition functions for linear molecules, J. Chem. Phys. 88 (1) (1988) 356–361.
[65] K. Huber, Molecular Spectra and Molecular Structure: IV. Constants of Diatomic Molecules, Springer Science & Business Media, 2013.
[66] J. Rogal, K. Reuter, Ab initio atomistic thermodynamics for surfaces: A primer, 2006.
[67] A. Reshak, Z. Alahmed, S. Auluck, A density functional study of the electronic properties of bismuth subcarbonate $Bi_2O_2CO_3$, Solid State Sci. 38 (2014) 138–142.
[68] T. Zhao, J. Zai, M. Xu, Q. Zou, Y. Su, K. Wang, X. Qian, Hierarchical $Bi_2O_2CO_3$ microspheres with improved visible-light-driven photocatalytic activity, Cryst. Eng. Comm. 13 (2011) 4010–4017.
[69] H. Cheng, B. Huang, K. Yang, Z. Wang, X. Qin, X. Zhang, Y. Dai, Facile template-free synthesis of $Bi_2O_2CO_3$ hierarchical microflowers and their associated photocatalytic activity, Chem.Phys. Chem. 11 (10) (2010) 2167–2173.
[70] W.L. Huang, First-principles determination of the absolute band-edge positions of BiOX (X=F, Cl, Br, I), Comput. Mater. Sci. 55 (2012) 166–170.
[71] K. Gao, Y.-J. Chen, Y. Ou, J.-m. Zeng, C. Hou, Y. Yang, Thickness-dependent surface reconstructions in non-van der Waals two-dimensional materials, Phys. Chem. Chem. Phys. 27 (1) (2025) 112–118.
[72] G.F. Cabeza, S.A. Fuente, C.I. Morgade, Exploring asymmetric and symmetric terminations of BiOX (001) surfaces via a DFT-based method: Influence of halogen identity (X=F, Cl, Br, I), Surf. Interfaces (2026) 109098.